IOP Publishing Plasma Physics and Controlled Fusion

Plasma Phys. Control. Fusion **56** (2014) 105005 (15pp) doi:10.1088/0741-3335/56/10/105005

On velocity-space sensitivity of fast-ion D-alpha spectroscopy

M Salewski[1], B Geiger[2], D Moseev[2,3], W W Heidbrink[4], A S Jacobsen[1], S B Korsholm[1], F Leipold[1], J Madsen[1], S K Nielsen[1], J Rasmussen[1], M Stejner[1], M Weiland[2] and the ASDEX Upgrade Team[2]

[1] Technical University of Denmark, Department of Physics, DK-2800 Kgs. Lyngby, Denmark
[2] Max-Planck-Institut für Plasmaphysik, D-85748 Garching, Germany
[3] FOM Institute DIFFER, 3430 BE Nieuwegein, The Netherlands
[4] University of California, Department of Physics and Astronomy, Irvine, CA 92697, USA

E-mail: msal@fysik.dtu.dk

Received 19 May 2014, revised 18 July 2014
Accepted for publication 13 August 2014
Published 8 September 2014

Abstract

The velocity-space observation regions and sensitivities in fast-ion D_α (FIDA) spectroscopy measurements are often described by so-called weight functions. Here we derive expressions for FIDA weight functions accounting for the Doppler shift, Stark splitting, and the charge-exchange reaction and electron transition probabilities. Our approach yields an efficient way to calculate correctly scaled FIDA weight functions and implies simple analytic expressions for their boundaries that separate the triangular observable regions in $(v_\parallel, v_\perp)$-space from the unobservable regions. These boundaries are determined by the Doppler shift and Stark splitting and could until now only be found by numeric simulation.

Keywords: fast-ion D-alpha spectroscopy, FIDA, charge-exchange recombination spectroscopy, fast ions, velocity space

(Some figures may appear in colour only in the online journal)

1. Introduction

Fast-ion D_α (FIDA) spectroscopy [1–3] is an application of charge-exchange recombination (CER) spectroscopy [4, 5] based on deuterium [6–11]. Deuterium ions in the plasma are neutralized in charge-exchange reactions with deuterium atoms from a neutral beam injector (NBI). The neutralized deuterium atoms are often in excited states, and hence they can emit D_α-photons which are Doppler-shifted due to the motion of the excited atoms. As the excited atoms inherit the velocities of the deuterium ions before the charge-exchange reaction, spectra of Doppler-shifted D_α-light are sensitive to the velocity distribution function of deuterium ions in the plasma. The measurement volume is given by the intersection of the NBI path and the line-of-sight of the CER diagnostic. D_α-photons due to bulk deuterium ions typically have Doppler shifts of about 1–2 nm whereas D_α-photons due to fast deuterium, which is the FIDA light, can have Doppler shifts of several nanometers. This paper deals with FIDA light but as the physics of D_α-light due to bulk deuterium ions is the same, our methods also apply to deuterium-based CER spectroscopy. The FIDA or CER-D_α light is sometimes obscured by Doppler shifted D_α-light from the NBI, unshifted D_α-light from the plasma edge, bremsstrahlung or line radiation from impurities.

FIDA spectra can be related to 2D velocity space by so-called weight functions [2, 3, 12]. Weight functions have been used in four ways: first, they quantify the velocity-space sensitivity of FIDA measurements, and hence they also separate the observable region in velocity space for a particular wavelength range from the unobservable region [2, 3, 13–29]. Second, they reveal how much FIDA light is emitted resolved in velocity space for a given fast-ion velocity distribution function [2, 3, 24–30]. The ions in the regions with the brightest FIDA light are then argued to dominate the measurement. Third, weight functions have been used to calculate FIDA spectra from given fast-ion velocity distribution functions [14, 31–33], eliminating the Monte-Carlo approach of the standard FIDA analysis code FIDASIM [34]. Fourth, recent tomographic inversion algorithms to infer 2D fast-ion velocity distribution

functions directly from the measurements rely heavily on weight functions [12, 31–33, 35].

Here we present a comprehensive discussion of FIDA weight functions and derive analytic expressions describing them. FIDA weight functions have often been presented in arbitrary units, relative units or without any units [2, 3, 15–28, 30] which is sufficient for their use as indicator of the velocity-space interrogation region or of the velocity-space origin of FIDA light. However, correctly scaled FIDA weight functions, which are necessary to calculate FIDA spectra or tomographic inversions, have only been implemented in the FIDASIM code recently [13, 14, 29, 31–33]. Weight functions are traditionally calculated using the FIDASIM code by computing the FIDA light from an ion on a fine grid in 2D velocity space and gyroangle. It is then counted how many photons contribute to a particular wavelength range for a given observation angle and point in velocity space using models for the Doppler shift, Stark splitting, charge-exchange probabilities and electron transition probabilities.

In section 2 we define weight functions and motivate their interpretation in terms of probabilities. Our viewpoint provides insights into functional dependencies between wavelength space and 2D velocity space that are not revealed by the traditional numerical calculation approach using FIDASIM. As a consequence we demonstrate how Doppler shift, Stark splitting, charge-exchange probabilities as well as the electron transition probabilities contribute to the velocity-space sensitivity of FIDA measurements. Section 3 focuses on weight functions implied by the Doppler shift alone as a relatively simple approximation. In section 4 we additionally treat Stark splitting and in section 5 the charge-exchange and the electron transition processes. In section 6 we present full FIDA weight functions accounting for these four effects. In section 7 we deduce exact analytic expressions for the boundaries of FIDA weight functions. We discuss the applicability of our results to CER spectroscopy and other fast-ion diagnostics in section 8 and conclude in section 9.

2. Definitions of weight functions

The velocity-space interrogation or observation regions of FIDA diagnostics are described by weight functions w_{vol} which are determined by charge-exchange probabilities, electron transition probabilities, Stark splitting and the Doppler shift. They thereby depend on position space and velocity space. Weight functions are defined to obey [2, 3, 12]

$$I(\lambda_1, \lambda_2, \phi) = \int_{\mathrm{vol}} \int_0^\infty \int_{-\infty}^\infty w_{\mathrm{vol}}(\lambda_1, \lambda_2, \phi, v_\parallel, v_\perp, \boldsymbol{x}) \times f(v_\parallel, v_\perp, \boldsymbol{x}) \mathrm{d}v_\parallel \mathrm{d}v_\perp \mathrm{d}\boldsymbol{x}. \quad (1)$$

$I(\lambda_1, \lambda_2, \phi)$ is the intensity of FIDA light in the wavelength range $\lambda_1 < \lambda < \lambda_2$ with a viewing angle ϕ between the line-of-sight of the FIDA diagnostic and the magnetic field. $(v_\parallel, v_\perp)$ denote velocities parallel and perpendicular to the magnetic field, respectively, and $\boldsymbol{x}$ denotes the spatial coordinates. Here we use $(v_\parallel, v_\perp)$-coordinates rather than the more widespread (E, p)-coordinates (energy, pitch) since our mathematical expressions are simpler in $(v_\parallel, v_\perp)$-coordinates. The energy and the pitch are defined as

$$E = \frac{1}{2} m_{\mathrm{D}} \left(v_\parallel^2 + v_\perp^2\right) \quad (2)$$

$$p = -\frac{v_\parallel}{v} \quad (3)$$

where m_{D} is the mass of a deuteron and $v = \sqrt{v_\parallel^2 + v_\perp^2}$ is the velocity magnitude. Note that the pitch is positive for co-current particles as usual. Key expressions are given in (E, p)-coordinates in the appendix. We assume $w_{\mathrm{vol}}(\lambda_1, \lambda_2, \phi, v_\parallel, v_\perp, \boldsymbol{x})$ and the fast-ion distribution function $f(v_\parallel, v_\perp, \boldsymbol{x})$ to be spatially uniform within the small measurement volume V. This may be violated near the foot of the pedestal where the density gradient length scale could be comparable with the mean free path of the emitters, but it should be fulfilled in the core plasma. With

$$w(\lambda_1, \lambda_2, \phi, v_\parallel, v_\perp) = V w_{\mathrm{vol}}(\lambda_1, \lambda_2, \phi, v_\parallel, v_\perp, \boldsymbol{x}) \quad (4)$$

equation (1) becomes

$$I(\lambda_1, \lambda_2, \phi) = \int_0^\infty \int_{-\infty}^\infty w(\lambda_1, \lambda_2, \phi, v_\parallel, v_\perp) f(v_\parallel, v_\perp) \mathrm{d}v_\parallel \mathrm{d}v_\perp. \quad (5)$$

Weight functions w relate the FIDA intensity $I(\lambda_1, \lambda_2, \phi)$ with units $[N_{\mathrm{ph}}/(\mathrm{s} \times \mathrm{sr} \times \mathrm{m}^2)]$ to the 2D fast-ion velocity distribution function with units $[N_{\mathrm{i}}/(\mathrm{m}^3 \times (\mathrm{m/s})^2)]$. The units of FIDA weight functions w are hence $[N_{\mathrm{ph}}/(\mathrm{s} \times \mathrm{sr} \times \mathrm{m}^2 \times N_{\mathrm{i}}/\mathrm{m}^3)]$, i.e. FIDA weight functions w quantify the *FIDA intensity per unit ion density* in the wavelength range $\lambda_1 < \lambda < \lambda_2$ for a viewing angle ϕ as a function of the ion velocity $(v_\parallel, v_\perp)$. The units of FIDA weight functions w_{vol} are $[N_{\mathrm{ph}}/(\mathrm{s} \times \mathrm{sr} \times \mathrm{m}^2 \times N_{\mathrm{i}})]$, i.e. the *FIDA intensity per ion* in $\lambda_1 < \lambda < \lambda_2$ for a viewing angle ϕ as function of $(v_\parallel, v_\perp)$. We will split FIDA weight functions w into a FIDA intensity function $R(v_\parallel, v_\perp)$ and a probability $\mathrm{prob}(\lambda_1 < \lambda < \lambda_2 | \phi, v_\parallel, v_\perp)$ according to

$$w(\lambda_1, \lambda_2, \phi, v_\parallel, v_\perp) = R(v_\parallel, v_\perp) \mathrm{prob}(\lambda_1 < \lambda < \lambda_2 | \phi, v_\parallel, v_\perp). \quad (6)$$

$R(v_\parallel, v_\perp)$ determines the total FIDA intensity for any wavelength of the photons per unit ion density. It depends only on the charge-exchange and electron transition processes, but not on the Doppler shift or Stark splitting that only change the wavelength of the photons. $\mathrm{prob}(\lambda_1 < \lambda < \lambda_2 | \phi, v_\parallel, v_\perp)$ determines the probability that a randomly selected detected photon has a wavelength in a particular range $\lambda_1 < \lambda < \lambda_2$ for a given projection angle ϕ and $(v_\parallel, v_\perp)$-coordinates. The conditioning symbol '|' means 'given'. The subject of this paper is the derivation of this probability. $\mathrm{prob}(\lambda_1 < \lambda < \lambda_2 | \phi, v_\parallel, v_\perp)$ depends on the Doppler shift and Stark Splitting as well as on the charge-exchange and electron transition processes which in turn all depend on the gyroangle γ of the ion at the time of the charge-exchange reaction. We treat $\gamma \in [0, 2\pi]$ as a random variable since we do not know the phases of all ions in the plasma, i.e. the initial conditions of any set of equations determining the ion motion are unknown as always in problems with a very large number of degrees of freedom. Since λ is determined by γ, it is also treated

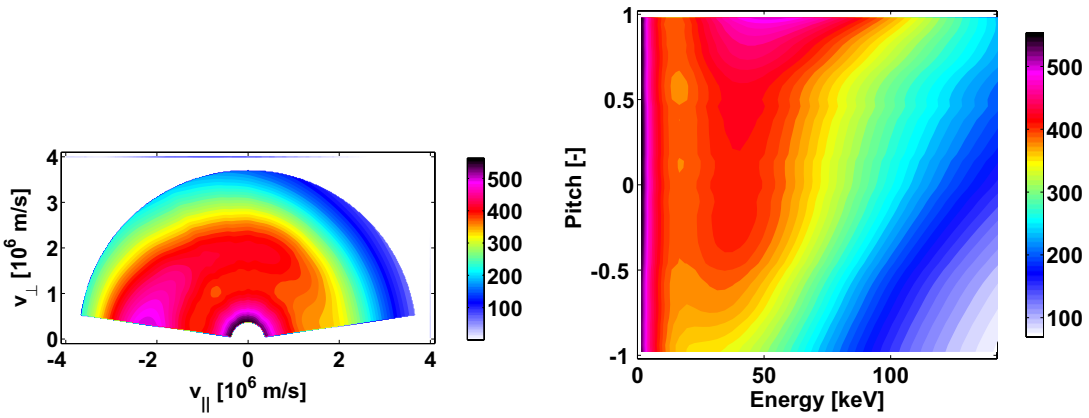

(a) (b)

Figure 1. The FIDA intensity function R shows the total FIDA intensity per unit ion density as function of (a) $(v_\parallel, v_\perp)$-coordinates and (b) (E, p)-coordinates. The units are $[N_{\mathrm{ph}}/(\mathrm{s} \times \mathrm{sr} \times \mathrm{m}^2 \times N_{\mathrm{i}}/\mathrm{m}^3)]$. The Balmer-alpha photons can have any Doppler-shifted wavelength. We computed R using FIDASIM for NBI Q3 at ASDEX Upgrade. Q3 has an injection energy of 60 keV.

as random variable. Probabilities are always dimensionless numbers in the interval [0,1], and hence the FIDA intensity function $R(v_\parallel, v_\perp)$ has the same units as weight functions.

$R(v_\parallel, v_\perp)$ is a common factor of all weight functions for a given ϕ at any wavelength. On the contrary, the probability function depends on the wavelength range and the projection angle ϕ and hence contains the spectral information. We compute $R(v_\parallel, v_\perp)$ using FIDASIM by modeling the charge-exchange and the electron transition processes. Examples of the FIDA intensity function for NBI Q3 at ASDEX Upgrade, which is used for FIDA measurements, are shown in figure 1(a) in $(v_\parallel, v_\perp)$-coordinates and in figure 1(b) in (E, p)-coordinates. The sensitivity of FIDA is low for very large ion energies where few photons are generated per ion. Ions with positive pitch generate more photons per ion than ions with negative pitch for Q3.

Usually one measures spectral or specific intensities I_λ, i.e. the intensity per wavelength with units $[N_{\mathrm{ph}}/(\mathrm{s} \times \mathrm{sr} \times \mathrm{m}^2 \times \mathrm{nm})]$. The intensity and the spectral intensity are related by

$$I(\lambda_1, \lambda_2, \phi) = \int_{\lambda_1}^{\lambda_2} I_\lambda(\lambda, \phi)\, \mathrm{d}\lambda. \tag{7}$$

The spectral intensity $I_\lambda(\lambda, \phi)$ can likewise be related to $f(v_\parallel, v_\perp)$ by a probability density function $\mathrm{pdf}(\lambda|\phi, v_\parallel, v_\perp)$ that then leads to a differential weight function $\mathrm{d}w$ as

$$I_\lambda(\lambda, \phi) = \int_0^\infty \int_{-\infty}^\infty \mathrm{d}w(\lambda, \phi, v_\parallel, v_\perp) f(v_\parallel, v_\perp)\, \mathrm{d}v_\parallel\, \mathrm{d}v_\perp \tag{8}$$

with

$$\mathrm{d}w(\lambda, \phi, v_\parallel, v_\perp) = R(v_\parallel, v_\perp)\mathrm{pdf}(\lambda|\phi, v_\parallel, v_\perp). \tag{9}$$

However, the weight functions we discuss here are related to a wavelength range rather than a particular wavelength since FIDA intensity measurements can only be made for a wavelength range and not for a single wavelength. Mathematically this is reflected in the always finite amplitudes of w whereas $\mathrm{d}w$ is singular at its boundary.

3. Doppler shift

An approximate shape of FIDA weight functions can be found by considering only the Doppler shift $\lambda - \lambda_0$ where $\lambda_0 = 656.1$ nm is the wavelength of the unshifted D_α-line and λ is the Doppler-shifted wavelength. In this section we derive this approximate shape by neglecting Stark splitting and by assuming that the D_α-photon emission is equally likely for all gyroangles γ of the ion at the time of the charge-exchange reaction. The probability density function in γ of randomly selected detected D_α photons is

$$\mathrm{pdf}_{\mathrm{D}_\alpha}(\gamma \mid v_\parallel, v_\perp) = 1/2\pi. \tag{10}$$

Stark splitting and an arbitrary $\mathrm{pdf}_{\mathrm{D}_\alpha}$ describing charge-exchange and electron transition probabilities will be introduced into the model in the next two sections. The Doppler shift depends on the projected velocity u of the ion along the line-of-sight according to

$$\lambda - \lambda_0 = u\lambda_0/c \tag{11}$$

where c is the speed of light. Equation (11) assumes $u \ll c$. Consider a gyrating ion with velocity $(v_\parallel, v_\perp)$ in a magnetic field. The ion is neutralized in a charge-exchange reaction which ultimately leads to emission of a D_α-photon. We define a coordinate system such that for $\gamma = 0$ the velocity vector of the ion is in the plane defined by the unit vector along the line-of-sight $\hat{\boldsymbol{u}}$ and $\boldsymbol{B}$ such that $\boldsymbol{v} \cdot \hat{\boldsymbol{u}} > 0$. Then the ion velocity is

$$\boldsymbol{v} = v_\parallel \hat{\boldsymbol{B}} + v_\perp \cos\gamma\, \hat{\boldsymbol{v}}_{\perp 1} - v_\perp \sin\gamma\, \hat{\boldsymbol{v}}_{\perp 2} \tag{12}$$

and the unit vector along the line-of-sight is

$$\hat{\boldsymbol{u}} = \cos\phi \hat{\boldsymbol{B}} + \sin\phi \hat{\boldsymbol{v}}_{\perp 1}. \tag{13}$$

The velocity component u of the ion along the line-of-sight at a projection angle ϕ to the magnetic field is then given by [12]

$$u = \boldsymbol{v} \cdot \hat{\boldsymbol{u}} = v_\parallel \cos\phi + v_\perp \sin\phi \cos\gamma. \tag{14}$$

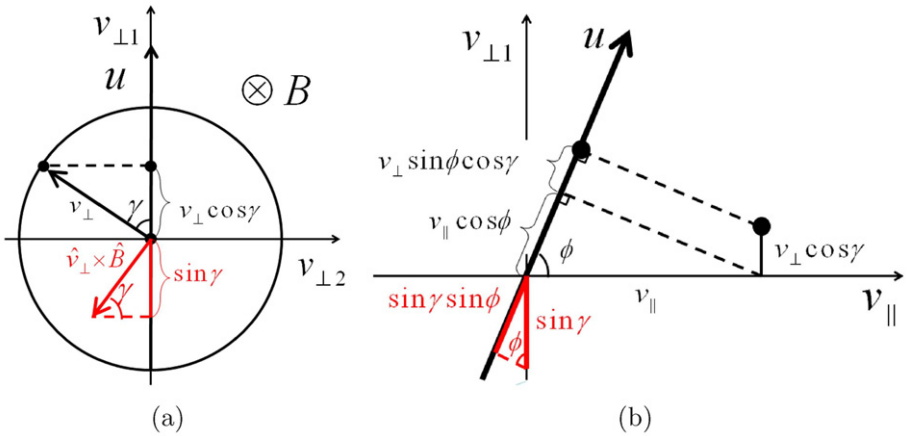

Figure 2. Projection of the ion velocity $(v_\parallel, v_\perp)$ and the unit vector $\hat{v} \times \hat{B}$ onto the line-of-sight. The latter is required for the treatment of Stark splitting discussed in section 4.

The projections of the ion velocity $\boldsymbol{v}$ and the unit vector $\hat{\boldsymbol{v}} \times \hat{\boldsymbol{B}}$ (relevant for Stark splitting) onto the line-of-sight in this coordinate system are illustrated in figure 2. Equation (14) shows that u is a random variable which depends on the random variable $\gamma \in [0, 2\pi]$. We now calculate the probability $\mathrm{prob}(u_1 < u < u_2|\phi, v_\parallel, v_\perp)$ that the ion has a projected velocity between u_1 and u_2 at the time of the charge-exchange reaction and therefore a Doppler-shifted D_α-line wavelength between λ_1 and λ_2 according to equation (11). For given $(v_\parallel, v_\perp)$ with $v_\perp \neq 0$ and projection angle $\phi \neq 0$, the projected velocity depends on the gyroangle γ. Conversely, we can calculate the gyroangles that lead to a given projected velocity u by solving equation (14) for γ:

$$\gamma = \arccos \frac{u - v_\parallel \cos\phi}{v_\perp \sin\phi}. \tag{15}$$

The arccos function is defined for $0 < \gamma < \pi$, and a second solution in $\pi < \gamma' < 2\pi$ is given by

$$\gamma' = 2\pi - \gamma. \tag{16}$$

Using equations (15) and (16) we can calculate gyroangles γ_1 and γ_2 and γ_1' and γ_2' corresponding to the limits u_1 and u_2 and transform the calculation of the probability to γ-space:

$$\begin{aligned}&\mathrm{prob}(u_1 < u < u_2|\phi, v_\parallel, v_\perp)\\ &= \mathrm{prob}(\gamma_2 < \gamma < \gamma_1|v_\parallel, v_\perp) + \mathrm{prob}(\gamma_1' < \gamma < \gamma_2'|v_\parallel, v_\perp)\\ &= \int_{\gamma_2}^{\gamma_1} \mathrm{pdf}_{D_\alpha}(\gamma \mid v_\parallel, v_\perp)\mathrm{d}\gamma + \int_{\gamma_1'}^{\gamma_2'} \mathrm{pdf}_{D_\alpha}(\gamma \mid v_\parallel, v_\perp)\,\mathrm{d}\gamma.\end{aligned} \tag{17}$$

As we here assume a uniform probability density, we can integrate equation (17) analytically:

$$\begin{aligned}\mathrm{prob}(u_1 < u < u_2|\phi, v_\parallel, v_\perp) &= \frac{\gamma_1 - \gamma_2}{2\pi} + \frac{\gamma_2' - \gamma_1'}{2\pi}\\ &= \frac{\gamma_1 - \gamma_2}{\pi}.\end{aligned} \tag{18}$$

The probability $\mathrm{prob}(u_1 < u < u_2|\phi, v_\parallel, v_\perp)$ is thus the fraction of the gyro-orbit that leads to a projected velocity between u_1 and u_2. Substitution of γ using equation (15) gives

$$\begin{aligned}&\mathrm{prob}(u_1 < u < u_2|\phi, v_\parallel, v_\perp)\\ &= \frac{1}{\pi}\left(\arccos\frac{u_1 - v_\parallel\cos\phi}{v_\perp\sin\phi} - \arccos\frac{u_2 - v_\parallel\cos\phi}{v_\perp\sin\phi}\right).\end{aligned} \tag{19}$$

Equation (19) is singular for $v_\perp = 0$ or $\phi = 0$. If $\phi = 0$, the projected velocity is just the parallel velocity as equation (14) reduces to $u = v_\parallel$. Then the probability function becomes

$$\mathrm{prob}(u_1 < u < u_2|\phi = 0, v_\parallel, v_\perp) = \begin{cases}1 & \text{for} \quad u_1 < v_\parallel < u_2\\ 0 & \text{otherwise}\end{cases} \tag{20}$$

which is identical to equation (19) in the limit $\phi \to 0$. For $v_\perp = 0$, i.e. on the $v_\parallel$-axis corresponding to ions not actually gyrating, equation (14) reduces to $u = v_\parallel \cos\phi$, and the probability function becomes

$$\begin{aligned}&\mathrm{prob}(u_1 < u < u_2|\phi, v_\parallel, v_\perp = 0)\\ &= \begin{cases}1 & \text{for} \quad u_1/\cos\phi < v_\parallel < u_2/\cos\phi\\ 0 & \text{otherwise.}\end{cases}\end{aligned} \tag{21}$$

Lastly, we note that the argument of the arccos function is often outside the range $[-1;1]$. In this case the arccos is complex, and we take the real part to obtain physically meaningful quantities. Equation (19) is a weight function describing just the projection onto the line-of-sight. We have previously derived the corresponding probability density function $\mathrm{pdf}(u|\phi, v_\parallel, v_\perp)$ to describe the velocity-space sensitivity of collective Thomson scattering (CTS) measurements [12]. The pdf can be found from the probability function by letting $u_1, u_2 \to u$:

$$\begin{aligned}\mathrm{pdf}(u|\phi, v_\parallel, v_\perp) &= \lim_{u_1, u_2 \to u} \frac{\mathrm{prob}(u_1 < u < u_2|\phi, v_\parallel, v_\perp)}{u_2 - u_1}\\ &= \frac{1}{\pi\, v_\perp \sin\phi \sqrt{1 - \left(\dfrac{u - v_\parallel\cos\phi}{v_\perp\sin\phi}\right)^2}}.\end{aligned} \tag{22}$$

Equations (19) to (22) have been used to interpret CTS measurements at TEXTOR [36] and should have great utility

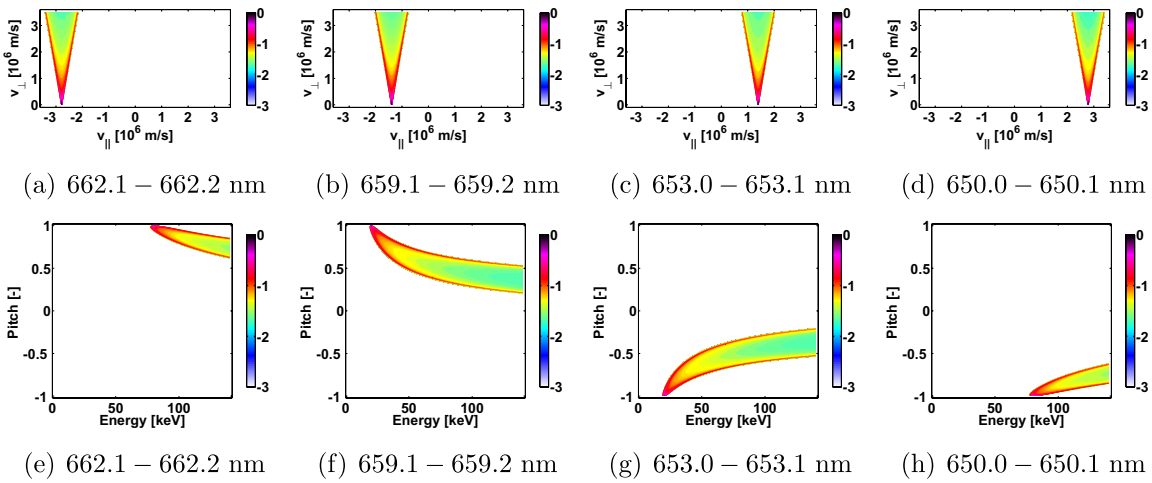

(a) $662.1 - 662.2$ nm (b) $659.1 - 659.2$ nm (c) $653.0 - 653.1$ nm (d) $650.0 - 650.1$ nm

(e) $662.1 - 662.2$ nm (f) $659.1 - 659.2$ nm (g) $653.0 - 653.1$ nm (h) $650.0 - 650.1$ nm

Figure 3. Probability functions after ((*a*)–(*d*)) equation (24) and ((*e*)–(*h*)) equation (68) for various Doppler shifts and a narrow wavelength range $\lambda_2 - \lambda_1 = 0.1$ nm. The projection angle is $\phi = 10^\circ$. The colorbar shows the base ten logarithm of the probability function $\log_{10}(\mathrm{prob}(\lambda_1 < \lambda < \lambda_2 | \phi, v_\parallel, v_\perp))$.

for CTS measurements at ASDEX Upgrade [37–39], LHD [40, 41] or ITER [42–44].

To obtain the probability function in λ-space, we first find the integration limits by substituting u in equation (15) using equation (11):

$$\gamma = \arccos \frac{c\left(\frac{\lambda}{\lambda_0} - 1\right) - v_\parallel \cos\phi}{v_\perp \sin\phi}. \tag{23}$$

Hence the probability function in λ-space becomes

$$\begin{aligned}\mathrm{prob}(\lambda_1 < \lambda < \lambda_2 | \phi, v_\parallel, v_\perp) &= \frac{\gamma_1 - \gamma_2}{\pi} \\ &= \frac{1}{\pi}\left(\arccos \frac{c\left(\frac{\lambda_1}{\lambda_0} - 1\right) - v_\parallel \cos\phi}{v_\perp \sin\phi}\right. \\ &\quad \left. - \arccos \frac{c\left(\frac{\lambda_2}{\lambda_0} - 1\right) - v_\parallel \cos\phi}{v_\perp \sin\phi}\right).\end{aligned} \tag{24}$$

This is a simple approximation to the probability part of FIDA weight functions neglecting Stark splitting and non-uniformity in $\mathrm{pdf}_{\mathrm{D}_\alpha}$ due to charge-exchange and electron transition probabilities.

Figures 3((*a*)–(*d*)) show $\mathrm{prob}(\lambda_1 < \lambda < \lambda_2 | \phi, v_\parallel, v_\perp)$ for a narrow wavelength range of 0.1 nm at various Doppler shifts. Figures 3((*e*)–(*h*)) show the corresponding probabilities $\mathrm{prob}(\lambda_1 < \lambda < \lambda_2 | \phi, E, p)$. The observable regions or interrogation regions are colored whereas the unobservable regions are white. The viewing angle is $\phi = 10^\circ$. The wavelength interval width $\lambda_2 - \lambda_1 = 0.1$ nm is comparable to the achievable spectral resolution of FIDA measurements at ASDEX Upgrade and is typical for tomographic measurements of 2D fast-ion velocity distribution functions [33]. The shape of the probability functions is triangular and symmetric in $(v_\parallel, v_\perp)$-coordinates, but the very tip of the triangle is cut off by the $v_\parallel$-axis as we will show more clearly in figure 5. The opening angle of the triangles is $2\phi = 20^\circ$ as the two sides have inclination angles of $\pm\phi$ with respect to the $v_\perp$-axis [12]. The location of the interrogation region changes substantially with the magnitude of the Doppler shift. In figures 3((*e*)–(*h*)) we show the same probability functions in (E, p)-coordinates since FIDA weight functions are traditionally given in these coordinates. The probability functions have more complicated shapes in (E, p)-coordinates. In figure 4 we vary the viewing angle ϕ. The larger the viewing angle, the larger the opening angle (2ϕ) of the triangular regions in $(v_\parallel, v_\perp)$-space, and the lower the probabilities that a detected photon has a wavelength in the particular wavelength range. These probabilities decrease for increasing projection angle ϕ since the spectrum of projected velocities of the ion and therefore wavelengths of the photons broaden according to equation (11) while the integral over the spectrum is the same. Figure 5 shows probability functions for broader wavelength ranges up to $\lambda_2 - \lambda_1 = 1$ nm typical for the traditional use of weight functions as sensitivity or signal origin indicators. The inclinations of the sides of the triangle are not affected by the larger wavelength range, but a larger tip of the triangle is now cut off by the $v_\parallel$-axis as figure 5(*d*) shows most clearly. The larger the wavelength range, the larger the probabilities become since larger fractions of the ion orbits can produce Doppler shifts within the wavelength limits. In the limit of wavelength ranges covering very large red- and blue-shifts, the probability function becomes unity. Figures 3–5 show that patterns in the velocity-space sensitivity of FIDA measurements are easier to spot in $(v_\parallel, v_\perp)$-space where FIDA weight functions always have triangular shapes.

Equations (14), (15) and (16) transform the problem of finding a probability in λ-space into the simpler problem of finding a probability in γ-space. We will use this transformation when we account for Stark splitting and non-uniform charge-exchange and electron transition probabilities in the next two sections.

4. Stark splitting

An electron Balmer alpha transition from the $n = 3$ to $n = 2$ state of a moving D-atom in the magnetic field of a tokamak leads to light emission at 15 distinct wavelengths

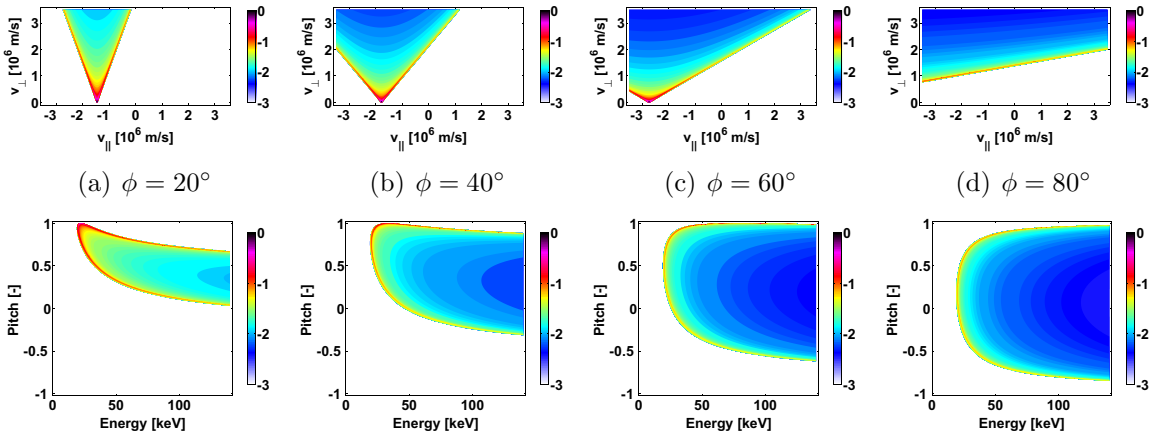

(a) $\phi = 20°$ (b) $\phi = 40°$ (c) $\phi = 60°$ (d) $\phi = 80°$

(e) $\phi = 20°$ (f) $\phi = 40°$ (g) $\phi = 60°$ (h) $\phi = 80°$

Figure 4. Probability functions after ((*a*)–(*d*)) equation (24) and ((*e*)–(*h*)) equation (68) for various projection angles ϕ and a narrow wavelength range $\lambda_2 - \lambda_1 = 659.1 - 659.0\,\text{nm} = 0.1\,\text{nm}$. The colorbar shows the base ten logarithm of the probability function $\log_{10}(\text{prob}(\lambda_1 < \lambda < \lambda_2 | \phi, v_\parallel, v_\perp))$.

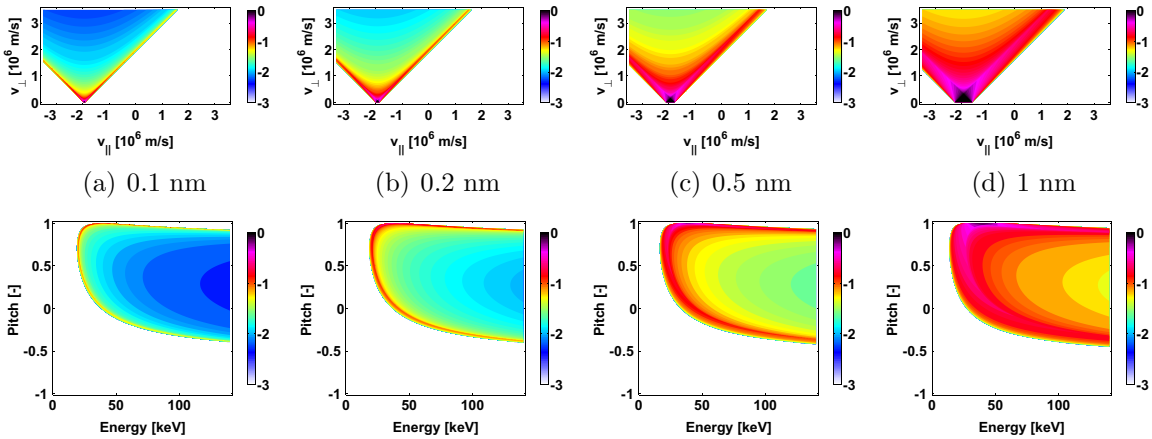

(a) 0.1 nm (b) 0.2 nm (c) 0.5 nm (d) 1 nm

(e) 0.1 nm (f) 0.2 nm (g) 0.5 nm (h) 1 nm

Figure 5. Probability functions after ((*a*)–(*d*)) equation (24) and ((*e*)–(*h*)) equation (68) for various wavelength ranges $\lambda_2 - \lambda_1$. The wavelength ranges are centered at 659.1 nm. The projection angle is $\phi = 45°$. The colorbar shows the base ten logarithm of the probability function $\log_{10}(\text{prob}(\lambda_1 < \lambda < \lambda_2 | \phi, v_\parallel, v_\perp))$.

λ_l. This is referred to as Stark splitting since the splitting occurs due to the electric field in the reference frame of the moving D-atom. Zeeman splitting is negligible in the analysis of FIDA measurements as it is much weaker than Stark splitting [34]. In this section we treat Stark splitting of the D_α-line. For this we find the integration limits for the 15 lines, find their probabilities and then sum over all possibilities. The magnitude of the Stark splitting wavelength shift is proportional to the magnitude of the electric field $\tilde{E}$ in the reference frame of the neutral:

$$\lambda_l = \lambda_0 + s_l \tilde{E} \tag{25}$$

where l is a number from 1 to 15 corresponding to the 15 lines and the constants s_l are [45, 46]

$$s_{l=1,\ldots,15} = \Big(-220.2, -165.2, -137.7, -110.2, -82.64, -55.1, -27.56, 0, 27.57, 55.15, 82.74, 110.3, 138.0, 165.6, 220.9 \Big) \times 10^{-18} \frac{\text{m}^2}{\text{V}}. \tag{26}$$

Lines 1, 4–6, 10–12 and 15 are so-called π-lines, and lines 2,3, 7–9, 13 and 14 are so-called σ-lines. Line 8 is the unshifted wavelength with $s_8 = 0$. The electric field $\tilde{\boldsymbol{E}}$ in the reference frame of the neutral is

$$\tilde{\boldsymbol{E}} = \hat{\boldsymbol{E}} + \boldsymbol{v} \times \boldsymbol{B}. \tag{27}$$

where $\hat{\boldsymbol{E}}$ is the electric field in the lab frame. In components this is

$$\begin{pmatrix} \tilde{E}_{\perp 1} \\ \tilde{E}_{\perp 2} \\ \tilde{E}_\parallel \end{pmatrix} = \begin{pmatrix} \hat{E}_{\perp 1} \\ \hat{E}_{\perp 2} \\ \hat{E}_\parallel \end{pmatrix} + \begin{pmatrix} v_\perp \cos\gamma \\ v_\perp \sin\gamma \\ v_\parallel \end{pmatrix} \times \begin{pmatrix} 0 \\ 0 \\ B \end{pmatrix} = \begin{pmatrix} \hat{E}_{\perp 1} + B v_\perp \sin\gamma \\ \hat{E}_{\perp 2} - B v_\perp \cos\gamma \\ \hat{E}_\parallel \end{pmatrix}. \tag{28}$$

The magnitude of the electric field in the frame of the neutral is

$$\tilde{E} = \sqrt{\hat{E}^2 + v_\perp^2 B^2 + 2 v_\perp B (\hat{E}_{\perp 1} \sin\gamma - \hat{E}_{\perp 2} \cos\gamma)}. \tag{29}$$

Suppose we make a FIDA measurement at a particular wavelength λ. The photon could have been emitted from any of the 15 lines with wavelength λ_l that is then Doppler shifted. Each of the 15 lines has a particular Stark wavelength shift corresponding to a particular Doppler shift with projected velocity u_l to be observable at λ. The 15 Doppler shift conditions are

$$\lambda = \lambda_l \left(1 + \frac{u_l}{c}\right) \tag{30}$$

which in combination with equation (25) yields

$$\lambda = \left(\lambda_0 + s_l \tilde{E}\right)\left(1 + \frac{u_l}{c}\right). \tag{31}$$

The projected velocity u_l and the electric field in the frame of the particle $\tilde{E}$ depend on the gyroangle. Substitution of $\tilde{E}$ using equation (29) and of u_l using equation (14) shows the relation between $\lambda, \phi, v_\perp, v_\parallel, \gamma_l$ and s_l:

$$\lambda = \left(\lambda_0 + s_l\sqrt{\hat{E}^2 + v_\perp^2 B^2 + 2v_\perp B(\hat{E}_{\perp 1}\sin\gamma_l - \hat{E}_{\perp 2}\cos\gamma_l)}\right) \times \left(1 + \frac{1}{c}\left(v_\parallel\cos\phi + v_\perp\sin\phi\cos\gamma_l\right)\right). \tag{32}$$

This relation describes not only the Doppler effect but also Stark splitting, the two effects changing the wavelength of a detectable photon. It can be used to transform integration limits in λ to γ-space where the integration is easier to do. Here we include Stark splitting neglecting any electric field in the laboratory frame of reference. This reveals the most important effects and is often a good approximation in a tokamak as $|\hat{E}| \ll |\boldsymbol{v} \times \boldsymbol{B}|$, in particular for fast ions with large $v_\perp$. In FIDASIM simulations this approximation is usually made. If there is no electric field in the laboratory reference frame, the electric field in the reference frame of the particle is

$$\tilde{E} = v_\perp B \tag{33}$$

and the Stark shift is just proportional to $v_\perp$:

$$\lambda_l = \lambda_0 + s_l v_\perp B. \tag{34}$$

The functional dependence between λ and γ in equation (32) simplifies, and λ becomes a cosine function of γ as in the relation between u and γ in equation (14). Equation (32) becomes

$$\lambda = (\lambda_0 + s_l v_\perp B)\left(1 + \frac{1}{c}\left(v_\parallel\cos\phi + v_\perp\sin\phi\cos\gamma_l\right)\right). \tag{35}$$

Equation (35) implies an equation for the exact shape of FIDA weight functions neglecting the electric field in the lab frame but accounting for Stark splitting as we will show in section 7. The inverse function is

$$\gamma_l = \arccos\frac{c\left(\frac{\lambda}{\lambda_0 + s_l v_\perp B} - 1\right) - v_\parallel\cos\phi}{v_\perp\sin\phi} \tag{36}$$

which gives a solution for $0 < \gamma < \pi$. A second solution is given by equation (16). These are integration limits in γ_l for each of the 15 lines. The relative intensities $I_l(\gamma)$ of π-lines and σ-lines depend on the gyroangle γ and can be written as [14]

$$\sigma : I_l(\gamma) = C_l(1 + \cos^2(\hat{\boldsymbol{u}}, \hat{\boldsymbol{v}} \times \hat{\boldsymbol{B}})) = C_l(1 + \sin^2\phi\sin^2\gamma) \tag{37}$$

$$\pi : I_l(\gamma) = C_l(1 - \cos^2(\hat{\boldsymbol{u}}, \hat{\boldsymbol{v}} \times \hat{\boldsymbol{B}})) = C_l(1 - \sin^2\phi\sin^2\gamma) \tag{38}$$

where $\hat{\boldsymbol{u}}$, $\hat{\boldsymbol{v}}$ and $\hat{\boldsymbol{B}}$ are unit vectors and the constants C_l are [14, 45, 47]

$$C_{l=1,\ldots,15} = \Big(1, 18, 16, 1681, 2304, 729, 1936, 5490, 1936, 729, 2304, 1681, 16, 18, 1\Big). \tag{39}$$

The expression of the projection of $\hat{\boldsymbol{v}} \times \hat{\boldsymbol{B}}$ onto the line-of-sight vector $\hat{\boldsymbol{u}}$ in terms of the gyroangle γ is illustrated in figure 2. The probabilities $\text{prob}(l|\gamma)$ that a detected photon comes from line l given the gyroangle γ can be calculated from the relative intensities:

$$\text{prob}(l|\gamma) = \frac{I_l(\gamma)}{\sum I_l(\gamma)}. \tag{40}$$

Since $\sum I_l(\gamma) = 18860$ is a constant independent of γ, we can write the probabilities of line l as

$$\text{prob}(l|\gamma) = \hat{C}_l(1 \pm \sin^2\phi\sin^2\gamma) \tag{41}$$

where the plus is used for the σ-lines and minus for the π-lines and

$$\hat{C}_l = \frac{C_l}{\sum_{n=1}^{15} C_l}. \tag{42}$$

The probability part of full FIDA weight functions accounting for Doppler and Stark effects for arbitrary $\text{pdf}_{\text{D}_\alpha}$ can now be calculated according to

$$\text{prob}(\lambda_1 < \lambda < \lambda_2|\phi, v_\parallel, v_\perp) = \sum_{l=1}^{15}\left(\int_{\gamma_{2,l}}^{\gamma_{1,l}} \text{prob}(l|\gamma)\text{pdf}_{\text{D}_\alpha}(\gamma \mid v_\parallel, v_\perp)\,\text{d}\gamma + \int_{\gamma'_{1,l}}^{\gamma'_{2,l}} \text{prob}(l|\gamma)\text{pdf}_{\text{D}_\alpha}(\gamma \mid v_\parallel, v_\perp)\,\text{d}\gamma\right). \tag{43}$$

We will discuss the nature of the $\text{pdf}_{\text{D}_\alpha}$ in FIDA measurements in the following section. Here we study basic effects by assuming a uniform $\text{pdf}_{\text{D}\alpha} = 1/(2\pi)$ for which we can solve the integrals in equation (43) analytically:

$$\begin{aligned}\text{prob}(\lambda_1 < \lambda < \lambda_2|\phi, v_\parallel, v_\perp) &= \sum_{l=1}^{15}\frac{1}{2\pi}\left(\int_{\gamma_{2,l}}^{\gamma_{1,l}} \hat{C}_l(1 \pm \sin^2\phi\sin^2\gamma)\,\text{d}\gamma + \int_{\gamma'_{1,l}}^{\gamma'_{2,l}} \hat{C}_l(1 \pm \sin^2\phi\sin^2\gamma)\,\text{d}\gamma\right)\\ &= \sum_{l=1}^{15}\hat{C}_l\left(\frac{\gamma_{1,l} - \gamma_{2,l}}{\pi} \pm \frac{\sin^2\phi}{2} \times\left(\frac{\gamma_{1,l} - \gamma_{2,l}}{\pi} - \frac{\sin(2\gamma_{1,l}) - \sin(2\gamma_{2,l})}{2\pi}\right)\right).\end{aligned} \tag{44}$$

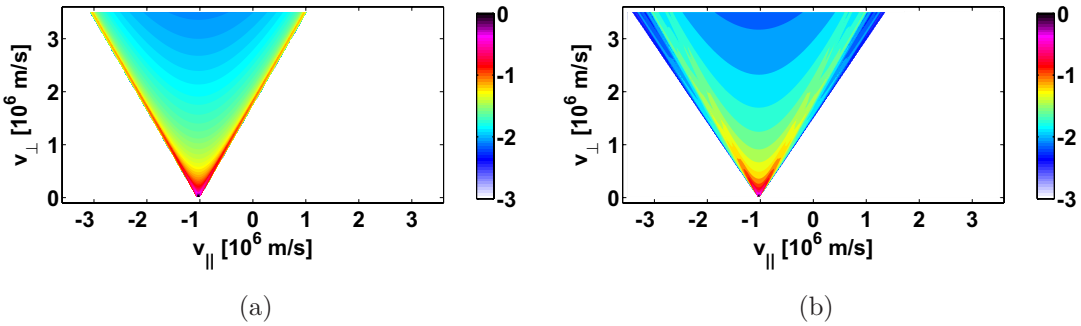

Figure 6. The probability functions $\mathrm{prob}(\lambda_1 < \lambda < \lambda_2 \mid \phi, v_\parallel, v_\perp)$ for $\mathrm{pdf}_{\mathrm{D}_\alpha} = 1/(2\pi)$: (*a*) without Stark splitting (equation (24)), (*b*) with Stark splitting (equation (44)). The wavelength range is $\lambda_2 - \lambda_1 = 0.1$ nm. The magnetic field is 1.74 T. The projection angle is $\phi = 30^\circ$. The colorbar shows the base ten logarithm of the probability part of the weight function $\log_{10}(\mathrm{prob}(\lambda_1 < \lambda < \lambda_2 | \phi, v_\parallel, v_\perp))$.

We leave the probability function in this form as substitution of the gyroangles using equation (36) provides no new insights. The probability function is calculated as a weighted sum over the 15 Stark splitting lines. The first fraction accounts for 15 different probability functions for the uniform distribution where the integration limits change for each Stark splitting line. The second term is a small correction due to the changing relative intensities of the 15 Stark splitting lines over the gyroangle. The corrections due to σ-lines and π-lines have different signs and hence partly cancel. For $\phi = 0$ this correction disappears.

Figure 6 demonstrates the effects of Stark splitting for a uniform $\mathrm{pdf}_{\mathrm{D}_\alpha}$ and a magnetic field of 1.74 T. The observation angle is $\phi = 30^\circ$ and the wavelength range is 658.0–658.1 nm in both figures. Stark splitting widens the interrogation region and changes the probabilities. The effect of the 15 Stark splitting lines shows most clearly close to the boundary of the observable region where several local maxima in the probability are formed. Since Stark splitting can be calculated accurately, it actually does not limit the spectral resolution of FIDA measurements as was sometimes asserted [3, 15, 16, 24, 48, 49] but rather just changes the velocity-space sensitivities.

5. Charge-exchange reaction and D_α-emission

The probability density $\mathrm{pdf}_{\mathrm{D}_\alpha}(\gamma \mid v_\parallel, v_\perp)$ is in fact not uniform as we assumed until now but is a complicated function depending on the charge-exchange probabilities and the electron transition probabilities and hence ultimately on the particular NBI as well as on the ion and electron temperatures and drift velocities. We hence find $\mathrm{pdf}_{\mathrm{D}_\alpha}(\gamma \mid v_\parallel, v_\perp)$ and the FIDA intensity per unit ion density $R(v_\parallel, v_\perp)$ irrespective of the detected wavelength by numeric computation using FIDASIM. Here we discuss the nature of these contributions.

The probability of a charge-exchange reaction between an ion and a neutral depends on their relative velocity as well as on the particular charge-exchange reaction. For an ion with given $(v_\parallel, v_\perp)$, the probability density of a charge-exchange reaction $\mathrm{pdf}_{\mathrm{CX}}(\gamma \mid v_\parallel, v_\perp)$ therefore depends on the gyroangle γ. Since FIDA light comes from a fast neutral that has been created from a fast ion in a charge-exchange reaction, FIDA does not sample the gyroangles of the ions uniformly, but favors those gyroangles for which the ion velocity vectors are similar to those of the neutrals. The charge-exchange probability density depends on the distribution of injected neutrals and halo neutrals and therefore on the particular NBI heating geometry.

The gyroangle probability densities that an ion at a particular gyroangle ultimately leads to a detection of a D_α-photon are further influenced by the electron transition probability densities $\mathrm{pdf}_{m\to n}(\gamma \mid v_\parallel, v_\perp)$ from energy level m to n. The $n = 3$ state can be populated and depopulated from any other energy state whereas only the $n = 3 \to 2$ leads to D_α-emission. These electron transition probabilities also depend on the velocity due to collisions. The probability density $\mathrm{pdf}_{\mathrm{D}_\alpha}(\gamma \mid v_\parallel, v_\perp)$ is hence found numerically using FIDASIM.

Before we proceed to such a full numeric computation of the relevant charge-exchange reactions and electron transitions, we study essential features using a simplified model. We consider the charge-exchange reaction

$$D^+ + D(n) \to D(n = 3) + D^+ \tag{45}$$

where the donor neutral $D(n)$ is in the nth excited state and the product neutral $D(n = 3)$ is in the $n = 3$ state and so can directly emit a D_α-photon. We emphasize that the $n = 3$ state can also be populated via any electron transition. However, in our simplified model we neglect electron transitions and consider only the direct population of the $n = 3$ state via the charge-exchange reaction. The charge-exchange reaction cross sections σ and the reactivities σv_{rel} strongly depend on the relative velocity v_{rel} which is usually expressed as the relative energy

$$E_{\mathrm{rel}} = \tfrac{1}{2} m_D v_{\mathrm{rel}}^2. \tag{46}$$

Figure 7 illustrates the cross sections σ_m and the reactivities $\sigma_m v_{\mathrm{rel}}$ for charge-exchange reactions with a donor neutral in state m directly resulting in an excited $n = 3$ neutral [14, 50–52]. In these reactions the donor neutral was in one of the first six excited states. The reactivities strongly depend on the relative velocities which in turn depend on the gyroangle. For simplicity, we treat a single source of injected neutrals neglecting that in reality there are sources at full, half and third injection energy. In the coordinate system from figure 2 the velocity of the beam neutrals is

$$\boldsymbol{v}_b = v_{b,\parallel}\hat{\boldsymbol{B}} + v_{b,\perp 1}\hat{\boldsymbol{v}}_{\perp 1} + v_{b,\perp 2}\hat{\boldsymbol{v}}_{\perp 2} \tag{47}$$

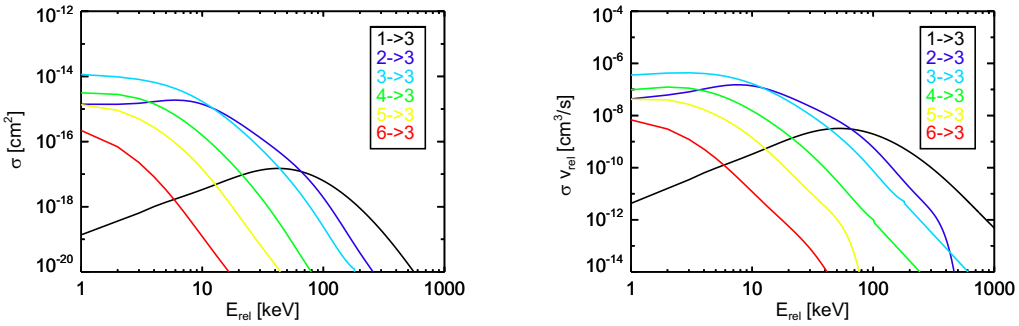

(a) Cross sections (b) σv_{rel}

Figure 7. Cross sections and reactivities $\sigma\, v_{\mathrm{rel}}$ of the charge-exchange reactions of ions with donor neutrals in the first six excited states directly resulting in an excited neutral in the $n = 3$ state.

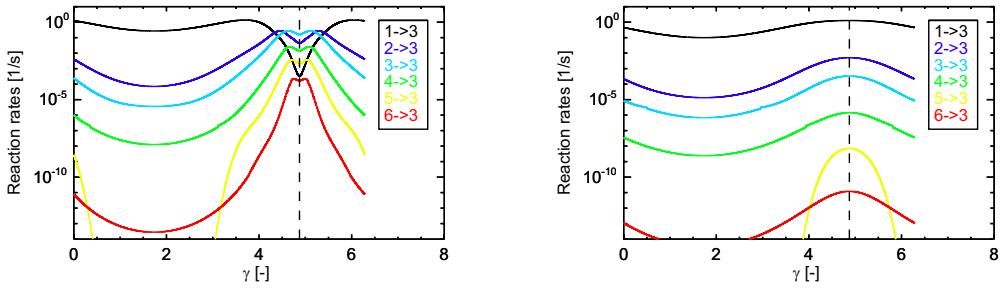

(a) $p = 0.5$ (b) $p = -0.5$

Figure 8. Reaction rates $\sigma_m v_{\mathrm{rel}} n_{\mathrm{neut},m}$ as function of the gyroangle γ for an energy of $E = 60\,\mathrm{keV}$ and pitches of $p = \pm 0.5$. The donor neutral population is here from the full injection energy peak of NBI Q3 while we neglect donor neutrals from half or third injection energies. Here we show rates for reactions with these beam neutrals in the first six excited states directly resulting in an excited neutral in the $n = 3$ state.

and the fast-ion velocity is given by equation (12). The relative velocity is then

$$v_{\mathrm{rel}} = \sqrt{(v_{b,\parallel} - v_{\parallel})^2 + (v_{b,\perp 1} - v_{\perp}\cos\gamma)^2 + (v_{b,\perp 2} - v_{\perp}\sin\gamma)^2}. \tag{48}$$

To find extremal values in v_{rel}, we set

$$\frac{\mathrm{d}v_{\mathrm{rel}}}{\mathrm{d}\gamma} = 0 \tag{49}$$

and find that the gyroangle γ is then given by

$$\tan\gamma = \frac{v_{b,\perp 2}}{v_{b,\perp 1}}. \tag{50}$$

If the reactivity $\sigma_m v_{\mathrm{rel}}$ were monotonic in the range of interest, the extrema of $\sigma_m v_{\mathrm{rel}}$ would correspond to the extrema of v_{rel}. However, figure 7 shows that the reactivities in particular of the charge-exchange reactions $1 \rightarrow 3$ and $2 \rightarrow 3$ are not monotonic but have maxima in the energy range of interest. Since the density of neutrals $n_{\mathrm{neut},m=1}$ in the first energy state is by far largest, this charge-exchange reaction often dominates. The reaction rates per ion are given by

$$r_m = \sigma_m v_{\mathrm{rel}} n_{\mathrm{neut},m}. \tag{51}$$

In figure 8 we show these reaction rates for the six charge-exchange reactions for an energy of $E = 60\,\mathrm{keV}$ and pitches of $p = \pm 0.5$. The reaction rates strongly depend on the gyroangle and have local maxima and minima. The dashed line shows the minima of the relative velocities given by equation (50) which coincides well with the local minima or maxima in the corresponding reaction rates. An extreme case is illustrated in figure 8(*a*) where the relative velocity goes to zero for a particular gyroangle. Figure 8(*b*) illustrates the reaction rates for velocity space coordinates far away from the donor neutral velocities.

Up to now we have not considered electron transition processes. In the following we calculate the full $\mathrm{pdf}_{\mathrm{D}\alpha}$ with FIDASIM where we model the important charge-exchange reactions and electron transitions as well as the beam geometry and energy distribution. Figure 9 shows such numerically calculated $\mathrm{pdf}_{\mathrm{D}\alpha}$ for a few energies and pitches. They often coarsely resemble phase-shifted cosine curves if one disregards local minima and maxima and Monte-Carlo noise. To study the effects of the non-uniform gyroangle distributions by simple models, we assume a model pdf to take the form

$$\mathrm{pdf}_{\mathrm{D}_\alpha}(\gamma \mid v_{\parallel}, v_{\perp}) = 1/2\pi + a\cos(\gamma + \bar{\gamma}) \tag{52}$$

where $a < 1/2\pi$ is an amplitude and $\bar{\gamma}$ is a phase shift. The integrals in equation (17) can be solved assuming $\mathrm{pdf}_{\mathrm{D}_\alpha}$ from

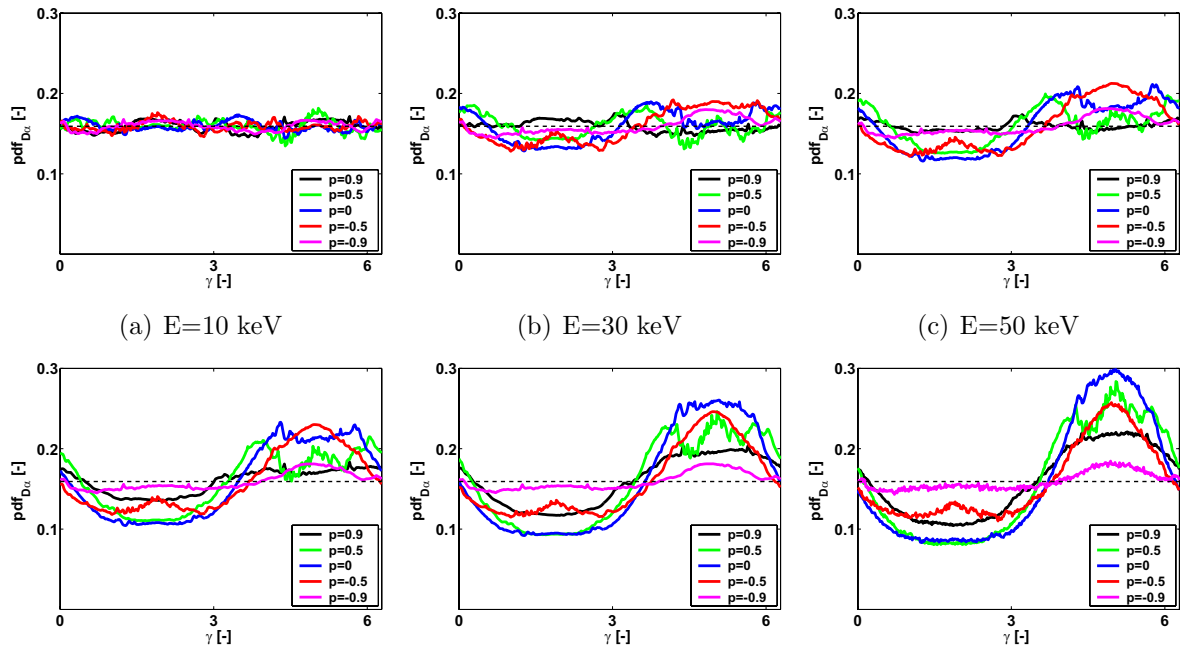

(a) E=10 keV (b) E=30 keV (c) E=50 keV

(d) E=70 keV (e) E=90 keV (f) E=110 keV

Figure 9. Probability density functions $\mathrm{pdf}_{\mathrm{D}_\alpha}$ at various positions in (E, p)-space (energy, pitch). The functions have been computed with FIDASIM. The NBI Q3 has an injection energy of 60 keV and an injection angle of about 120°. The thin dashed line is the uniform distribution assumed up to now.

equation (52):

$$\begin{aligned}
&\mathrm{prob}(\lambda_1 < \lambda < \lambda_2 \mid \phi, v_\parallel, v_\perp) \\
&\quad = \int_{\gamma_2}^{\gamma_1} 1/2\pi + a\cos(\gamma + \bar{\gamma})\,\mathrm{d}\gamma \\
&\qquad + \int_{\gamma_1'}^{\gamma_2'} 1/2\pi + a\cos(\gamma + \bar{\gamma})\,\mathrm{d}\gamma \\
&\quad = \frac{\gamma_1 - \gamma_2}{\pi} + 2a\cos\bar{\gamma}\Big(\sin\gamma_1 - \sin\gamma_2\Big). \qquad (53)
\end{aligned}$$

Again we leave the probability function in this form and do not substitute the gyroangles. The first term in equation (53) also appears for the uniform pdf whereas the second term accounts for cosine shape. It is proportional to the amplitude a and to the cosine of the phase shift $\cos\bar{\gamma}$. We can also integrate our model pdf accounting for Stark splitting. Equation (43) becomes

$$\begin{aligned}
&\mathrm{prob}(\lambda_1 < \lambda < \lambda_2 | \phi, v_\parallel, v_\perp) \\
&= \sum_{l=1}^{15}\Bigg(\int_{\gamma_{2,l}}^{\gamma_{1,l}} \hat{C}_l\Big(1 \pm \sin^2\phi\sin^2\gamma\Big) \\
&\quad \times\Big(\frac{1}{2\pi} + a\cos(\gamma + \bar{\gamma})\Big)\,\mathrm{d}\gamma \\
&\quad + \int_{\gamma_{1,l}'}^{\gamma_{2,l}'} \hat{C}_l\Big(1 \pm \sin^2\phi\sin^2\gamma\Big)\Big(\frac{1}{2\pi} + a\cos(\gamma + \bar{\gamma})\Big)\,\mathrm{d}\gamma\Bigg) \\
&= \sum_{l=1}^{15}\hat{C}_l\Bigg(\frac{\gamma_{1,l} - \gamma_{2,l}}{\pi} \pm \frac{\sin^2\phi}{2} \\
&\quad \times\Bigg(\frac{\gamma_{1,l} - \gamma_{2,l}}{\pi} - \frac{\sin(2\gamma_{1,l}) - \sin(2\gamma_{2,l})}{2\pi}\Bigg) \\
&\quad + 2a\cos\bar{\gamma}\Bigg(\sin\gamma_{1,l} - \sin\gamma_{2,l} \pm \frac{\sin^2\phi}{3} \\
&\quad \times\Big(\sin^3\gamma_{1,l} - \sin^3\gamma_{2,l}\Big)\Bigg)\Bigg). \qquad (54)
\end{aligned}$$

Equation (54) contains all terms of equation (44) as well as the term accounting for the cosine shape from equation (53). Additionally, another correction term arises accounting for changing intensities of the Stark splitting lines and varying amplitude due to the cosine function. This term has again different signs for σ-lines and π-lines and disappears for $\phi = 0$.

As already mentioned, the phase shift $\bar{\gamma}$ in equation (52) can be found approximately from geometric considerations. Further, we construct a model for the amplitude so that it increases with energy and decreases with the magnitude of the pitch as motivated by figure 9 where these trends appear:

$$a = \frac{E}{E_0}(1 - p^2) = \frac{v_\perp^2}{v_{\perp 0}^2}. \qquad (55)$$

This model for the amplitude has E_0 as the only free parameter. It has units of energy to non-dimensionalize the energy coordinate. The amplitude a of the cosine function in equation (52) is inversely proportional to E_0. For $E_0 = 1$ MeV the amplitudes of the probability density functions roughly correspond to the FIDASIM calculation over the relevant energy range up to 90 keV as we show in figure 10. Figure 11 shows that the typical large-scale cosine-like shape of $\mathrm{pdf}_{\mathrm{D}_\alpha}$ leads to lopsided probabilities. In this particular case ions close to the right side of the triangular weight functions have higher

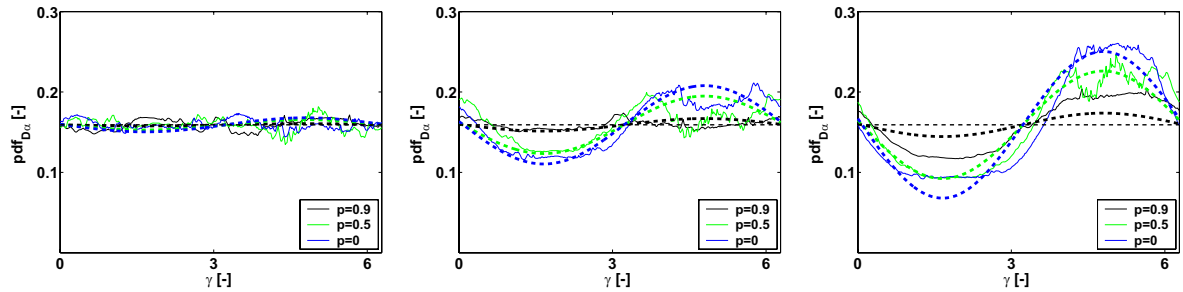

(a) E=10 keV (b) E=50 keV (c) E=90 keV

Figure 10. Comparison of $\mathrm{pdf}_{\mathrm{D}_\alpha}$ as computed with FIDASIM with the cosine model $\mathrm{pdf}_{\mathrm{D}_\alpha}$ (equation (52)) at various positions in velocity space. The thick dashed lines are the model cosine, and the thin dashed line is the uniform distribution.

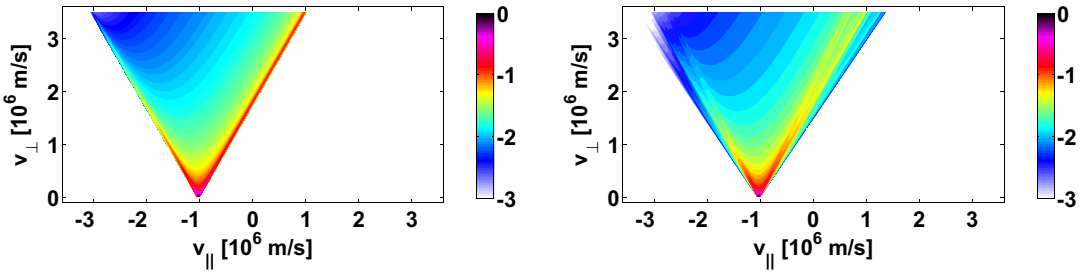

(a) (b)

Figure 11. The probability functions $\mathrm{prob}(\lambda_1 < \lambda < \lambda_2 \mid \phi, v_\parallel, v_\perp)$ for $\mathrm{pdf}_{\mathrm{D}_\alpha}$ given by equation (52): (*a*) without Stark splitting (equation (53)), (*b*) with Stark splitting (equation (54)). The wavelength range is $\lambda_2 - \lambda_1 = 0.1$ nm. The magnetic field is 1.74 T. The projection angle is $\phi = 30°$. The colorbar shows the base ten logarithm of the probability part of the weight function $\log_{10}(\mathrm{prob}(\lambda_1 < \lambda < \lambda_2 | \phi, v_\parallel, v_\perp))$.

probabilities to emit light in the particular wavelength range than those close to the left side of the triangle. The phase angle $\bar{\gamma}$ determines how lopsided the probability function becomes. In figure 11(*a*) we show one of the extreme cases as $\cos(\bar{\gamma}) = 1$. For $\cos(\bar{\gamma}) = 0$ the probability function is symmetric and the same as that for the uniform distribution. Figure 11(*b*) shows the probability function for the model $\mathrm{pdf}_{\mathrm{D}_\alpha}$ given by equation (52) and accounting for Stark splitting. The effect of Stark splitting is similar to that observed for the uniform $\mathrm{pdf}_{\mathrm{D}_\alpha}$. Lastly, we note that any arbitrary $\mathrm{pdf}_{\mathrm{D}_\alpha}$ can be expanded into a Fourier series and then analytical, smooth FIDA weight functions could be constructed from the Fourier components which each can be integrated as in equation (54).

6. Full FIDA weight functions

Substitution of equation (43) into equation (6) gives an analytic expression for full FIDA weight functions accounting for Doppler and Stark effects and allowing for arbitrary $\mathrm{pdf}_{\mathrm{D}\alpha}$:

$$w(\lambda_1, \lambda_2, \phi, v_\parallel, v_\perp) = R(v_\parallel, v_\perp) \times \sum_{l=1}^{15} \left(\int_{\gamma_{2,l}}^{\gamma_{1,l}} \mathrm{prob}(l|\gamma) \mathrm{pdf}_{\mathrm{D}_\alpha}(\gamma \mid v_\parallel, v_\perp)\, \mathrm{d}\gamma + \int_{\gamma'_{1,l}}^{\gamma'_{2,l}} \mathrm{prob}(l|\gamma) \mathrm{pdf}_{\mathrm{D}_\alpha}(\gamma \mid v_\parallel, v_\perp)\, \mathrm{d}\gamma \right). \quad (56)$$

Equation (56) is general whereas the assumptions of the FIDASIM code are used to calculate R and $\mathrm{pdf}_{\mathrm{D}_\alpha}$ [14, 34]. In particular, the calculation of the weight functions assumes that the FIDA emission comes from a small volume in configuration space. Practically, R and $\mathrm{pdf}_{\mathrm{D}_\alpha}$ are calculated from the distribution function $f_{\mathrm{D}_\alpha}(\gamma \mid v_\parallel, v_\perp)$ of the FIDA intensity per unit ion density over γ which we calculate numerically using FIDASIM. Then

$$R(v_\parallel, v_\perp) = \int_0^{2\pi} f_{\mathrm{D}_\alpha}(\gamma \mid v_\parallel, v_\perp)\, \mathrm{d}\gamma, \quad (57)$$

$$\mathrm{pdf}_{\mathrm{D}_\alpha}(\gamma \mid v_\parallel, v_\perp) = \frac{f_{\mathrm{D}_\alpha}(\gamma \mid v_\parallel, v_\perp)}{R(v_\parallel, v_\perp)}. \quad (58)$$

We prefer not to substitute equation (58) into equation (56) to emphasize that R is a factor common to any weight function with any wavelength range. We compare full FIDA weight functions as computed with our formalism with the traditional weight function as computed with FIDASIM in figure 12. The two approaches give the same result within small and controllable discretization errors and Monte Carlo noise from the sampling of the neutral beam particles in FIDASIM below 5%. This shows that our new formalism is consistent with the traditional FIDASIM computation as expected since the physics assumptions are the same. However, our approach provides additional insight into functional dependencies not revealed by the traditional brute-force computation. It also leads to faster computations if weight functions in several wavelength ranges are to be computed since the time-consuming collisional–radiative model only has to be evaluated once to find R and pdf_{D_α}, and weight functions

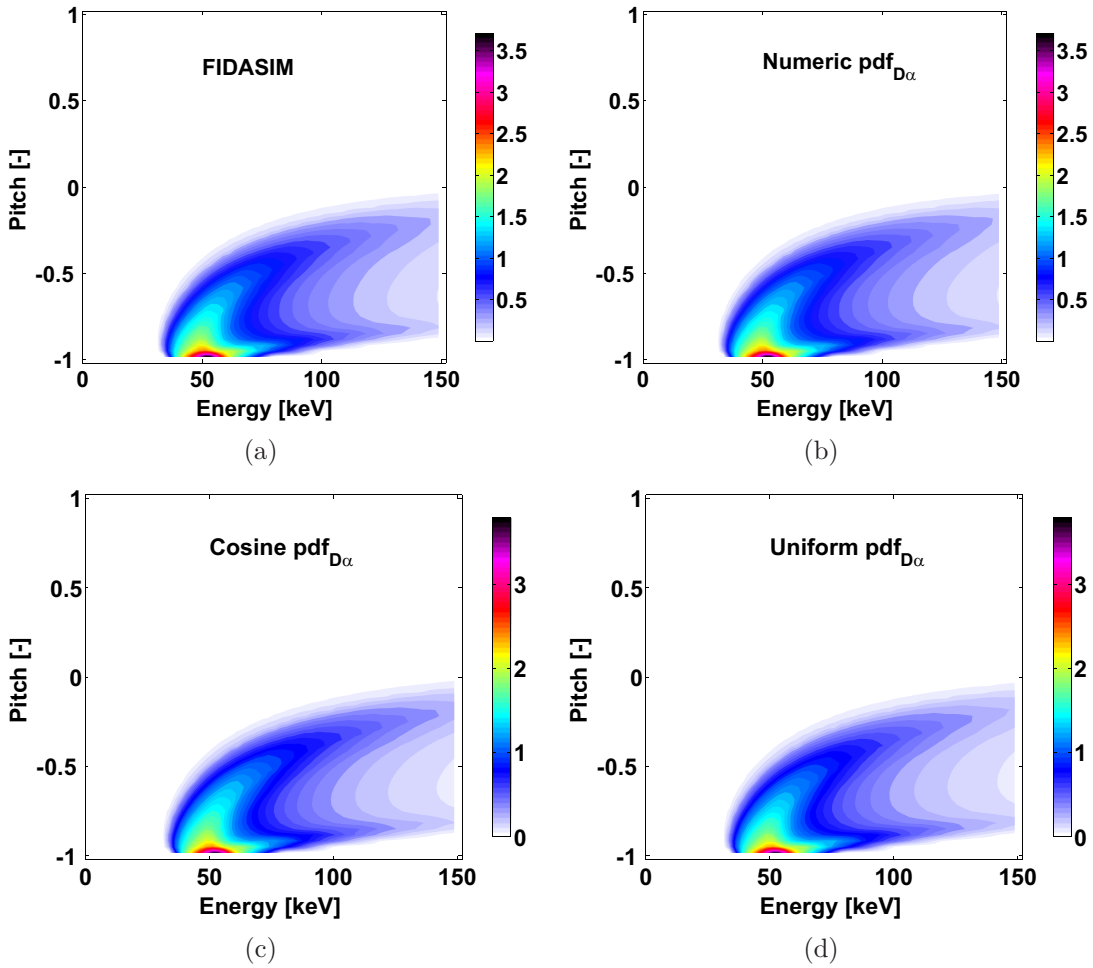

Figure 12. Full FIDA weight functions as computed with (*a*) traditional FIDASIM, (*b*) equation (56) for numerically computed $\mathrm{pdf}_{\mathrm{D}_\alpha}$ using FIDASIM, (*c*) equation (56) for the cosine model $\mathrm{pdf}_{\mathrm{D}_\alpha}$, (*d*) equation (56) for the uniform model $\mathrm{pdf}_{\mathrm{D}_\alpha}$. The projection angle is $\phi = 155^\circ$. The wavelength range is 660–661 nm. The magnetic field is 1.74 T.

for any wavelength range can then be computed rapidly using equation (56). Additionally, we compare these full FIDA weight functions based on numerically computed $\mathrm{pdf}_{\mathrm{D}_\alpha}$ using FIDASIM with full weight functions given by the uniform $\mathrm{pdf}_{\mathrm{D}_\alpha}$ and the cosine $\mathrm{pdf}_{\mathrm{D}_\alpha}$ which match the full computation to within 20%.

7. Boundaries of FIDA weight functions

Often it is useful to know the velocity-space interrogation regions of FIDA measurements. Until now these observable regions in velocity space had to be found by numerical simulations with the FIDASIM code. Here we show that these velocity-space interrogation regions are in fact completely determined by a simple analytic expression accounting for the Doppler shift and Stark splitting. The boundaries of FIDA weight functions are found by solving equation (35) for $v_\parallel$ and setting $\cos\gamma = \pm 1$ and $l = 1$ or $l = 15$ which gives the largest possible Doppler shift and Stark splitting wavelength shift, respectively. The boundaries for arbitrary l are

$$v_\parallel = \pm v_\perp \tan\phi + \frac{c}{\cos\phi}\left(\frac{\lambda}{\lambda_0 + s_l v_\perp B} - 1\right). \qquad (59)$$

This is a hyperbolic equation. Nevertheless, for $v_\perp \ll c$ we have $s_l v_\perp B \ll \lambda_0$, and we can expand the right hand side in a Taylor series:

$$v_\parallel \approx \left(\pm\tan\phi - \frac{c}{\cos\phi}\frac{\lambda}{\lambda_0}\frac{s_l B}{\lambda_0}\right) v_\perp + \frac{c}{\cos\phi}\frac{\lambda-\lambda_0}{\lambda_0}. \qquad (60)$$

For $v_\perp \ll c$ the FIDA weight functions are thus approximately bounded by straight lines in $(v_\parallel, v_\perp)$-coordinates. The $v_\parallel$-intercept is $\frac{c}{\cos\phi}\frac{\lambda-\lambda_0}{\lambda_0}$ and the slope is given by the term in the bracket. In figure 13 we compare the outer boundary given by equation (60) with the corresponding FIDA weight function in (E, p)-coordinates. The outermost boundaries are found for $l = 1$ and $l = 15$. However, since the outermost three lines on each side correspond to Stark lines with tiny intensities (see equation (39)), the effective boundaries of the velocity-space interrogation region could be considered to be defined by $l = 4$ and $l = 12$ as indicated by dashed lines. Stark splitting has always been neglected in previous work where boundaries of weight functions or minimum energies below which the weight function is zero have been discussed [2, 3, 15, 16, 18, 19, 22, 28]. Figure 13 demonstrates that the effect of Stark splitting can be substantial as it decreases the minimum energy below which the weight function is zero by

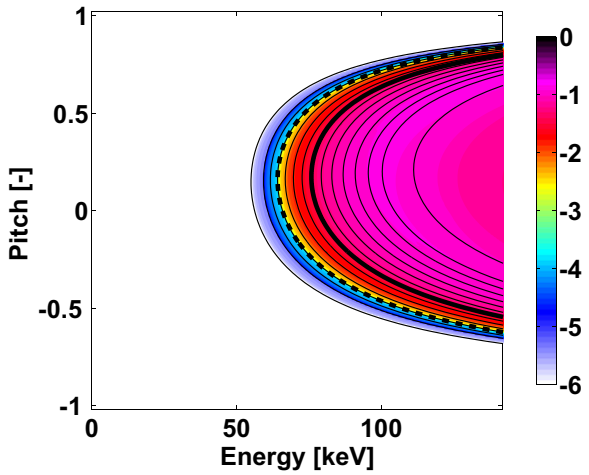

Figure 13. Boundaries of a FIDA weight function compared with the corresponding weight function for $\phi = 80^\circ$, 662–663 nm, and $B = 1.74$ T. For each of the 15 Stark splitting lines there is a boundary shown by thin black lines. The thick black line denotes $l = 8$ (no Stark shift). The thick dashed black lines denote $l = 4$ and $l = 12$. Note that here we show probabilities down to 10^{-6}.

10–20 keV depending on whether we define the boundary by $l = 1, 15$ or by $l = 4, 12$. In Figure 13 the thick lines correspond to previous models with no Stark splitting (here $l = 8$). The outermost lines set the interrogation region accounting for Stark splitting ($l = 1, 15$), and dashed lines correspond to the Stark lines $l = 4, 12$.

8. Discussion

8.1. Fast-ion studies

ASDEX Upgrade has five FIDA views. Correctly scaled FIDA weight functions, as we present here, allow measurements of 2D fast-ion velocity distribution functions by tomographic inversion [33]. This will allow velocity-space studies of fast-ion distributions which are generated by up to 20 MW of neutral beam injection power and 6 MW of ion cyclotron heating power [53–55]. Moreover, weight functions are not specific to FIDA and have also been given for CTS [12], neutron count rate measurements [2], neutral particle analyzers (NPAs) [2], fast-ion loss detectors [56], neutron spectroscopy [57, 58] and beam emission spectroscopy [59]. If weight functions for the other diagnostics are correctly scaled, as those for FIDA and CTS [12], the fast-ion diagnostics can be combined in joint measurements of 2D fast-ion velocity distribution functions using the available diagnostics [32]. For example, ASDEX Upgrade is equipped with fast-ion loss detectors (FILD) [26, 60, 61], fast-ion D_α (FIDA) [13, 27, 29, 33], CTS [31, 32, 37–39, 62, 63], neutron energy spectrometry [64, 65], NPAs [66, 67], and γ-ray spectrometry [68].

8.2. CER spectroscopy of the bulk ions

Weight functions describing FIDA diagnostics will also describe D_α-based CER spectroscopy of the bulk deuterium ions [6–11] and would then also be applicable to CER spectroscopy based on impurity species [4, 5] if the path of the emitter from the charge-exchange reaction to the photon emission does not curve significantly. Hence we could also show velocity-space interrogation regions of particular wavelength intervals in CER spectroscopy with our approach, estimate where in velocity space most signal comes for a given ion velocity distribution function, calculate spectra, and—perhaps the most interesting application—calculate velocity-space tomographies of bulk-ion velocity distribution functions of the emitting species. A temperature, density and drift parallel to the magnetic field could be found by fitting a 2D Maxwellian to the tomography of the ion distribution functions, and this could provide an alternative to standard methods. This method would be even more interesting if parallel and perpendicular ion temperatures are discrepant as sometimes observed in MAST [69] or JET [70] or if the ions do not have a Maxwellian distribution.

9. Conclusions

The velocity-space sensitivity of FIDA measurements can be described by weight functions. We derive correctly scaled expressions for FIDA weight functions accounting for the Doppler shift, Stark splitting, and the charge-exchange and the electron transition probabilities. Our approach provides insight not revealed by the traditional numerical computation of weight functions implemented in the FIDASIM code. By using simple analytic models we show how these physical effects contribute to the velocity-space sensitivities of FIDA measurements. The Doppler shift determines an approximate shape of the observable region in $(v_\parallel, v_\perp)$-space which is triangular and mirror symmetric. Stark splitting broadens this triangular observable region whereas the charge-exchange and electron transition probabilities do not change the boundaries of FIDA weight functions separating the observable region from the unobservable region in velocity space. Our approach implies exact analytic expressions for these boundaries that take Stark splitting into account and therefore differ by up to 10–20 keV in (energy, pitch)-space from similar expressions in previous work. We show that Stark splitting changes the sensitivity of the measurement, but this does not limit the achievable spectral resolution of FIDA measurements as has sometimes been asserted [3, 15, 16, 24, 48, 49]. Weight functions as we deduce here can be used to rapidly compute synthetic FIDA spectra from a 2D velocity distribution function. This lays the groundwork for the solution of the inverse problem to determine 2D velocity distribution functions from FIDA measurements. Lastly, our methods are immediately applicable to charge-exchange recombination spectroscopy measurements of D_α-light from the bulk deuterium population to determine their temperature and drift velocity as well as any anisotropy.

Acknowledgments

Dmitry Moseev was supported by an EFDA fellowship. This work has received funding from the European Union's Horizon 2020 research and innovation program under grant agreement number 633053. The views and opinions expressed herein do not necessarily reflect those of the European Commission.

Appendix

Here we give key expressions in the widespread (E, p)-coordinates (Energy, pitch) that are used in the TRANSP code. They can be obtained by substituting

$$v_\parallel = -p\sqrt{2E/m} \tag{61}$$

$$v_\perp = \sqrt{(1-p^2)2E/m} \tag{62}$$

into the corresponding expressions in $(v_\parallel, v_\perp)$-coordinates. Weight functions in (E, p)-coordinates are defined as

$$I(\lambda_1, \lambda_2, \phi) = \int\int\int w(\lambda_1, \lambda_2, \phi, E, p) f(E, p)\, \mathrm{d}E\, \mathrm{d}p. \tag{63}$$

They can be written as

$$w(\lambda_1, \lambda_2, \phi, E, p) = R(E, p)\mathrm{prob}(\lambda_1 < \lambda < \lambda_2|\phi, E, p). \tag{64}$$

The projected velocity u along the line-of-sight is

$$u = \Big(-p\cos\phi + \sqrt{1-p^2}\sin\phi\cos\gamma\Big)\sqrt{2E/m}. \tag{65}$$

If there is no static electric field, the observed wavelength as function of gyroangle becomes

$$\lambda = \Big(\lambda_0 + s_l B\sqrt{(1-p^2)2E/m}\Big) \times \left(1 + \frac{1}{c}(-p\cos\phi + \sqrt{1-p^2}\sin\phi\cos\gamma_l)\sqrt{2E/m}\right) \tag{66}$$

and the inverse function is

$$\gamma_l = \arccos \frac{\frac{c}{\sqrt{2E/m}}\left(\frac{\lambda}{\lambda_0 + s_l B\sqrt{(1-p^2)2E/m}} - 1\right) + p\cos\phi}{\sqrt{1-p^2}\sin\phi}. \tag{67}$$

The probability function for a uniform gyroangle distribution and no Stark splitting becomes

$$\mathrm{prob}(\lambda_1 < \lambda < \lambda_2|\phi, E, p) = \frac{1}{\pi}\left(\arccos\frac{\frac{c}{\sqrt{2E/m}}\left(\frac{\lambda_1}{\lambda_0} - 1\right) + p\cos\phi}{\sqrt{1-p^2}\sin\phi} - \arccos\frac{\frac{c}{\sqrt{2E/m}}\left(\frac{\lambda_2}{\lambda_0} - 1\right) + p\cos\phi}{\sqrt{1-p^2}\sin\phi}\right) \tag{68}$$

and the pdf is expressed in (E, p) as

$$\mathrm{pdf}(\lambda, \phi, E, p) = \frac{1}{\pi\sqrt{2E/m(1-p^2)}\sin\phi\sqrt{1 - \left(\frac{\frac{c}{\sqrt{2E/m}}\left(\frac{\lambda_1}{\lambda_0} - 1\right) + p\cos\phi}{\sqrt{1-p^2}\sin\phi}\right)^2}}. \tag{69}$$

For an arbitrary gyroangle distribution and no Stark splitting the probability function becomes

$$\mathrm{prob}(\lambda_1 < \lambda < \lambda_2|\phi, E, p) = \int_{\gamma_{2,l}}^{\gamma_{1,l}} \mathrm{pdf}_{\mathrm{D}_\alpha}(\gamma \mid E, p)\, \mathrm{d}\gamma + \int_{\gamma'_{1,l}}^{\gamma'_{2,l}} pdf_{\mathrm{D}_\alpha}(\gamma \mid E, p)\, \mathrm{d}\gamma. \tag{70}$$

The general expression of the probability function for an arbitrary gyroangle distribution and accounting for Stark splitting is

$$\mathrm{prob}(\lambda_1 < \lambda < \lambda_2|\phi, E, p) = \sum_{l=1}^{15}\left(\int_{\gamma_{2,l}}^{\gamma_{1,l}} \mathrm{prob}(l|\gamma)\mathrm{pdf}_{\mathrm{D}_\alpha}(\gamma \mid E, p)\, \mathrm{d}\gamma + \int_{\gamma'_{1,l}}^{\gamma'_{2,l}} \mathrm{prob}(l|\gamma)\mathrm{pdf}_{\mathrm{D}_\alpha}(\gamma \mid E, p)\, \mathrm{d}\gamma\right). \tag{71}$$

The general expression of FIDA weight functions is

$$w(\lambda_1, \lambda_2, \phi, E, p) = R(E, p) \times \sum_{l=1}^{15}\left(\int_{\gamma_{2,l}}^{\gamma_{1,l}} \mathrm{prob}(l|\gamma)\mathrm{pdf}_{\mathrm{D}_\alpha}(\gamma \mid E, p)\, \mathrm{d}\gamma + \int_{\gamma'_{1,l}}^{\gamma'_{2,l}} \mathrm{prob}(l|\gamma)\mathrm{pdf}_{\mathrm{D}_\alpha}(\gamma \mid E, p)\, \mathrm{d}\gamma\right) \tag{72}$$

and their boundaries are given by

$$E = \frac{mc^2(\lambda - \lambda_0)^2}{2(1-p^2) \times \left(\lambda_0\cos\phi\left(\pm\tan\phi - p + \frac{c\lambda s_l B}{\lambda_0^2\cos\phi}\right)\right)^2}. \tag{73}$$

References

[1] Heidbrink W W, Burrell K H, Luo Y, Pablant N A and Ruskov E 2004 *Plasma Phys. Control. Fusion* **46** 1855–75

[2] Heidbrink W W, Luo Y, Burrell K H, Harvey R W, Pinsker R I and Ruskov E 2007 *Plasma Phys. Control. Fusion* **49** 1457–75

[3] Heidbrink W W 2010 *Rev. Sci. Instrum.* **81** 10D727

[4] Fonck R, Darrow D and Jaehnig K 1984 *Phys. Rev.* A **29** 3288–309

[5] Isler R C 1994 *Plasma Phys. Control. Fusion* **36** 171

[6] Busche E, Euringer H and Jaspers R 1997 *Plasma Phys. Control. Fusion* **39** 1327–38

[7] Pütterich T, Wolfrum E, Dux R and Maggi C 2009 *Phys. Rev. Lett.* **102** 025001

[8] Grierson B A, Burrell K H, Solomon W M and Pablant N A 2010 *Rev. Sci. Instrum.* **81** 10D735

[9] Grierson B A, Burrell K H, Chrystal C, Groebner R J, Kaplan D H, Heidbrink W W, Muñoz Burgos J M, Pablant N A, Solomon W M and Van Zeeland M A 2012 *Rev. Sci. Instrum.* **83** 10D529

[10] Grierson B A, Burrell K H, Heidbrink W W, Lanctot M J, Pablant N A and Solomon W M 2012 *Phys. Plasmas* **19** 056107

[11] Grierson B, Burrell K, Solomon W, Budny R and Candy J 2013 *Nucl. Fusion* **53** 063010

[12] Salewski M *et al* 2011 *Nucl. Fusion* **51** 083014

[13] Geiger B *et al* 2014 *Nucl. Fusion* **54** 022005

[14] Geiger B 2013 Fast-ion transport studies using FIDA spectroscopy at the ASDEX Upgrade tokamak *PhD Thesis* Ludwig-Maximilians-Universität München

[15] Heidbrink W W, Bell R E, Luo Y and Solomon W 2006 *Rev. Sci. Instrum.* **77** 10F120

[16] Luo Y, Heidbrink W W, Burrell K H, Kaplan D H and Gohil P 2007 *Rev. Sci. Instrum.* **78** 033505

[17] Podestà M, Heidbrink W W, Bell R E and Feder R 2008 *Rev. Sci. Instrum.* **79** 10E521

[18] Van Zeeland M A, Heidbrink W W and Yu J H 2009 *Plasma Phys. Control. Fusion* **51** 055001

[19] Van Zeeland M *et al* 2010 *Nucl. Fusion* **50** 084002
[20] Bortolon A, Heidbrink W W and Podestà M 2010 *Rev. Sci. Instrum.* **81** 10D728
[21] Heidbrink W W, McKee G R, Smith D R and Bortolon A 2011 *Plasma Phys. Control. Fusion* **53** 085007
[22] Michael C A *et al* 2013 *Plasma Phys. Control. Fusion* **55** 095007
[23] Jones O M *et al* and the MAST Team 2014 arXiv:1401.6864
[24] Heidbrink W W, Luo Y, Muscatello C M, Zhu Y and Burrell K H 2008 *Rev. Sci. Instrum.* **79** 10E520
[25] Podesta M *et al* 2009 *Phys. Plasmas* **16** 056104
[26] Garcia-Munoz M *et al* 2011 *Nucl. Fusion* **51** 103013
[27] Geiger B, Garcia-Munoz M, Heidbrink W W, McDermott R M, Tardini G, Dux R, Fischer R and Igochine V 2011 *Plasma Phys. Control. Fusion* **53** 065010
[28] Muscatello C M, Heidbrink W W, Kolesnichenko Y I, Lutsenko V V, Van Zeeland M A and Yakovenko Y V 2012 *Plasma Phys. Control. Fusion* **54** 025006
[29] Geiger B, Dux R, McDermott R M, Potzel S, Reich M, Ryter F, Weiland M, Wünderlich D and Garcia-Munoz M 2013 *Rev. Sci. Instrum.* **84** 113502
[30] Pace D C *et al* 2013 *Phys. Plasmas* **20** 056108
[31] Salewski M *et al* 2012 *Nucl. Fusion* **52** 103008
[32] Salewski M *et al* 2013 *Nucl. Fusion* **53** 063019
[33] Salewski M *et al* 2014 *Nucl. Fusion* **54** 023005
[34] Heidbrink W, Liu D, Luo Y, Ruskov E and Geiger B 2011 *Commun. Comput. Phys.* **10** 716–41
[35] Salewski M *et al* 2014 Doppler tomography in fusion plasmas and astrophysics, submitted
[36] Nielsen S K *et al* 2011 *Nucl. Fusion* **51** 063014
[37] Meo F *et al* 2008 *Rev. Sci. Instrum.* **79** 10E501
[38] Salewski M *et al* 2010 *Nucl. Fusion* **50** 035012
[39] Meo F *et al* and the ASDEX Upgrade Team 2010 *J. Phys.: Conf. Ser.* **227** 012010
[40] Kubo S *et al* 2010 *Rev. Sci. Instrum.* **81** 10D535
[41] Nishiura M *et al* 2014 *Nucl. Fusion* **54** 023006
[42] Salewski M, Meo F, Bindslev H, Furtula V, Korsholm S B, Lauritzen B, Leipold F, Michelsen P K, Nielsen S K and Nonbø l E 2008 *Rev. Sci. Instrum.* **79** 10E729
[43] Salewski M, Eriksson L G, Bindslev H, Korsholm S, Leipold F, Meo F, Michelsen P and Nielsen S 2009 *Nucl. Fusion* **49** 025006
[44] Salewski M *et al* 2009 *Plasma Phys. Control. Fusion* **51** 035006
[45] Schrödinger E 1926 *Ann. Phys.* **385** 437–90
[46] Epstein P 1926 *Phys. Rev.* **28** 695–710
[47] Foster J S and Chalk L 1929 *Proc. R. Soc.* A **123** 108–18
[48] Luo Y, Heidbrink W W and Burrell K H 2004 *Rev. Sci. Instrum.* **75** 3468–70
[49] Muscatello C M, Heidbrink W W, Taussig D and Burrell K H 2010 *Rev. Sci. Instrum.* **81** 10D316
[50] 2012 www.adas.ac.uk
[51] Janev R K and Smith J J 1993 *Atomic and Plasma–Material Interaction Data for Fusion* vol 4 (Vienna: IAEA)
[52] Janev R K, Reiter D and Samm U *Technical Report* Jül- 4105 Forschungszentrum Jülich
[53] Gruber O *et al* 2007 *Nucl. Fusion* **47** S622–34
[54] Kallenbach A *et al* 2012 *IEEE Trans. Plasma Sci.* **40** 605–13
[55] Stroth U *et al* 2013 *Nucl. Fusion* **53** 104003
[56] Pace D C *et al* 2012 *Rev. Sci. Instrum.* **83** 073501
[57] Jacobsen A S *et al* 2014 Velocity-space sensitivity of neutron emission spectrometry, in preparation
[58] Jacobsen A S *et al* 2014 *Rev. Sci. Instrum.* **85** 11E103
[59] Pace D, Pinsker R, Heidbrink W, Fisher R, Van Zeeland M, Austin M, McKee G and García-Muñoz M 2012 *Nucl. Fusion* **52** 063019
[60] García-Muñoz M, Martin P, Fahrbach H U, Gobbin M, Günter S, Maraschek M, Marrelli L, Zohm H and the ASDEX Upgrade Team 2007 *Nucl. Fusion* **47** L10–15
[61] García-Muñoz M *et al* 2009 *Nucl. Fusion* **49** 085014
[62] Furtula V, Salewski M, Leipold F, Michelsen P K, Korsholm S B, Meo F, Moseev D, Nielsen S K, Stejner M and Johansen T 2012 *Rev. Sci. Instrum.* **83** 013507
[63] Furtula V, Leipold F, Salewski M, Michelsen P K, Korsholm S B, Meo F, Moseev D, Nielsen S K, Stejner M and Johansen T 2012 *J. Instrum.* **7** C02039
[64] Giacomelli L, Zimbal A, Tittelmeier K, Schuhmacher H, Tardini G and Neu R 2011 *Rev. Sci. Instrum.* **82** 123504
[65] Tardini G, Zimbal A, Esposito B, Gagnon-Moisan F, Marocco D, Neu R, Schuhmacher H and the ASDEX Upgrade Team 2012 *J. Instrum.* **7** C03004
[66] Kurki-Suonio T, Hynönen V, Suttrop W, Fahrbach H U, Stober J and the ASDEX Upgrade Team 2006 *Europhysics Conference Abstracts* vol 30I, p P2.145
[67] Äkäslompolo S, Hirvijoki E, Kurki-Suonio T and the ASDEX Upgrade Team 2010 *Europhysics Conference Abstracts* vol 34A, p P5.113
[68] Nocente M *et al* 2012 *Nucl. Fusion* **52** 094021
[69] Hole M J, von Nessi G, Fitzgerald M, McClements K G and Svensson J 2011 *Plasma Phys. Control. Fusion* **53** 074021
[70] von Hellermann M G, Core W G F, Frieling J, Horton L D, Konig R W T, Mandl W and Summers H P 1993 *Plasma Phys. Control. Fusion* **35** 799–824